

# Liquid-activated quantum emission from native hBN defects for nanofluidic sensing

# Liquid-activated quantum emission from native hBN defects for nanofluidic sensing

**Nathan Ronceray[1,2,*], Yi You[3,4], Evgenii Glushkov[1], Martina Lihter[1], Benjamin Rehl[2], Tzu-Heng Chen[1], Gwang-Hyeon Nam[3,4], Kenji Watanabe[5], Takashi Taniguchi[6], Sylvie Roke[2], Ashok Keerthi[3,4], Jean Comtet[7], Boya Radha[3,4,*], and Aleksandra Radenovic[1,*]**

[1]Laboratory of Nanoscale Biology, Institute of Bioengineering (IBI), School of Engineering (STI), École Polytechnique Fédérale de Lausanne (EPFL), Lausanne, Switzerland.
[2]Laboratory for fundamental BioPhotonics, IBI, STI, EPFL, Lausanne, Switzerland
[3]Department of Physics and Astronomy, School of Natural Sciences, The University of Manchester, Manchester, United Kingdom
[4]National Graphene Institute, University of Manchester, Manchester, United Kingdom
[5]Research Center for Functional Materials, National Institute for Materials Science, 1-1 Namiki, Tsukuba, Japan
[6]International Center for Materials Nanoarchitectonics, National Institute for Materials Science, 1-1 Namiki, Tsukuba, Japan
[7]Soft Matter Science and Engineering Laboratory, ESPCI Paris, Université PSL, Sorbonne Université, CNRS UMR 7615, France
[*]nathan.ronceray@epfl.ch, radha.boya@manchester.ac.uk, aleksandra.radenovic@epfl.ch

## Summary

Nanostructures made of two-dimensional (2D) materials have become the flagship of nanofluidic discoveries in recent years[1,2]. By confining liquids down to a few atomic layers, anomalies in molecular transport[3–5] and structure[6,7] have been revealed. Currently, only indirect and ensemble averaged techniques have been able to operate in such extreme confinements, as even the smallest molecular fluorophores are too bulky to penetrate state-of-the-art single-digit nanofluidic systems[8]. This strong limitation calls for the development of novel optical approaches allowing for the direct molecular imaging of liquids confined at the nanoscale. Here, we show that native defects present at the surface of hexagonal boron nitride[9] (hBN) - a widely used 2D material - can serve as probes for molecular sensing in liquid, without compromising the atomic smoothness of their host material. We first demonstrate that native surface defects are readily activated through interactions with organic solvents and confirm their quantum emission properties. Vibrational spectra of the emitters suggest that their activation occurs through the chemisorption of carbon-bearing liquid molecules onto native hBN defects. The correlated activation of neighboring defects reveals single-molecule dynamics at the interface, while defect emission spectra offer a direct readout of the local dielectric properties of the liquid medium. We then harvest these effects in atomically smooth slit-shaped van der Waals channels, revealing molecular dynamics and increasing dielectric order under nanometre-scale confinement. Liquid-activated native defects in pristine hBN bridge the gap between solid-state nanophotonics and nanofluidics and open up new avenues for nanoscale sensing and optofluidics.

## Main

Fluorescent defect centers in wide band-gap materials like diamond, silicon carbide or boron nitride have received increasing attention in recent years as they allow to probe nanoscale matter through interactions with their dipoles and electron spins[10,11]. In particular, a variety of point defects with energy levels well within the 6 eV band gap of hexagonal boron nitride (hBN) were

found to be promising for their room-temperature quantum emission properties[12–14]. While the material engineering toolbox has been widely used to artificially induce quantum emitters in hBN by irradiation[15,16], strain engineering[17] or carbon doping[18,19], liquid treatments have been left relatively unexplored. In recent works, we combined liquid and irradiation treatments, to demonstrate that plasma-induced hBN surface defects can be activated by water[20] and binary mixtures of water with organic solvents[21], while liquid post-treatment of ion beam-exposed hBN can modify its defect emission properties[22]. Additionally, plasma-induced surface defects were found to report on single interfacial charge dynamics such as proton hopping[20,21]. However, even mild plasma treatment induces mechanical and chemical changes, yielding hBN crystals which no longer possess atomically smooth surfaces[23], and preventing the integration of defects in ultra-flat van der Waals heterostructures which are currently driving progress in angstrom-scale fluidics[4,7].

Here, we report that common organic solvents can activate visible-range quantum emission from native surface defects in high-quality pristine hBN crystals. This phenomenon relies on the interaction of organic molecules with pre-existing surface defects in high-quality hBN crystals[9,24–26]. Using spectral super-resolution microscopy[27], we reveal defect-mediated molecular random walks as well as couplings between defect dipoles and the liquid medium leading to the dielectric liquid tuning of the emission wavelength. By relying only on intrinsic properties of a widely used two-dimensional material and common solvents, the fluorescence activation mechanism reported here is then used to image nanofluidic structures, with defects acting as nanoscale probes of the order and dynamics of liquid media confined down to the nanoscale.

## Liquid-activated fluorescence from hBN native defects

We observed that untreated hBN crystals become fluorescent when brought in contact with most common organic solvents like ethanol. To demonstrate this effect, we exfoliated high-quality hBN crystals[24] using the scotch-tape method onto a glass coverslip, which was then used to seal a liquid-filled chamber placed on an inverted microscope. As sketched in Fig. 1a, the hBN crystal photoluminescence (PL) under 561 nm wide-field laser light illumination (0.35-3.5 kW/cm$^2$) was collected through the coverslip by a high-numerical aperture objective and projected onto a camera chip. As we previously reported, pristine hBN in air or water does not exhibit fluorescence under these illumination conditions[20]. However, we observed that as-exfoliated crystals in contact with ethanol exhibited an intense fluorescence signal (Fig. 1b). The fluorescence intensity gradually decreased under continuous illumination, and stabilized after several seconds, revealing emission from sub-diffraction spots as shown in Fig. 1c and in supplementary movie 1. We attribute this emission to defects present in the as-exfoliated crystal and activated through contact with the liquid. These defects can be super-resolved using single-molecule localization microscopy: each active defect can be localized with an uncertainty $\sigma_{\text{loc}} \sim \sigma_{\text{PSF}}/\sqrt{N_{\text{loc}}}$, where $\sigma_{\text{PSF}}$ is the radial extent of the microscope point spread function ($\approx 110$ nm) and $N_{\text{loc}}$ is the number of photons counted in the diffraction-limited spot. It the imaging conditions used here, we obtain localization uncertainties in the range of $10-20$ nm. Emitters are randomly distributed on the basal plane of the crystal (Fig. S1), and the strategies for controlling their position by limiting the exposed surface are discussed later in the manuscript. As characterized in Fig. 1d, the number of emitters responsible for the emission decreased under constant illumination and reached a stable value of $\sim$0.5 emitters per square micron in ethanol. We verified that this process does not deteriorate the crystal and the decrease shown in Fig. 1c is reversible: when left in the dark, the crystal fluorescence recovers within tens of minutes, as shown in Fig. S4.

This fluorescent activation of native defects was found to occur for most common organic solvents, such as n-alkanes (pentane to hexadecane) and primary alcohols (methanol to 1-pentanol). However, we did not observe any emission in pure water, heavy water, and hydrogen peroxide. For quantitative comparison, we imaged freshly cleaved hBN crystals under the same illumination conditions, but exposed to different liquid media such as water, glycerol (Gly), ethylene glycol (EG), benzyl alcohol (BA), dimethylsolfoxide (DMSO), ethanol (EtOH), dichloromethane (DCM), chloroform (CF) and cyclohexane (CH). The steady state fluorescence under these solvents can be quantified by crystal brightness $I_{\text{crystal}}$ defined as the sum of localized emitter intensities per surface unit and time unit (Fig. 1e). Based on these observations, we can define three classes of solvents depending on the extent of hBN defect activation. Intense fluorescence was obtained ($I_{\text{crystal}} > 5 \times 10^2$photons/$\mu$m$^2$/s) for most

organic solvents such as primary alcohols, n-alkanes and chloroalkanes (type I). Prototypical high-boiling point ($\geq 200^{\circ}C$) liquids such as glycerol exhibited only a limited but well measurable defect activation (type II). For water, no fluorescence was observed (type III). The difference between defect activation types could not be explained merely by physical parameters of the solvent (Fig. S2), pointing at chemical specificity. The steady-state emitter density was found to depend on the illumination intensity as well as on the liquid medium (Fig. S3 & S5).

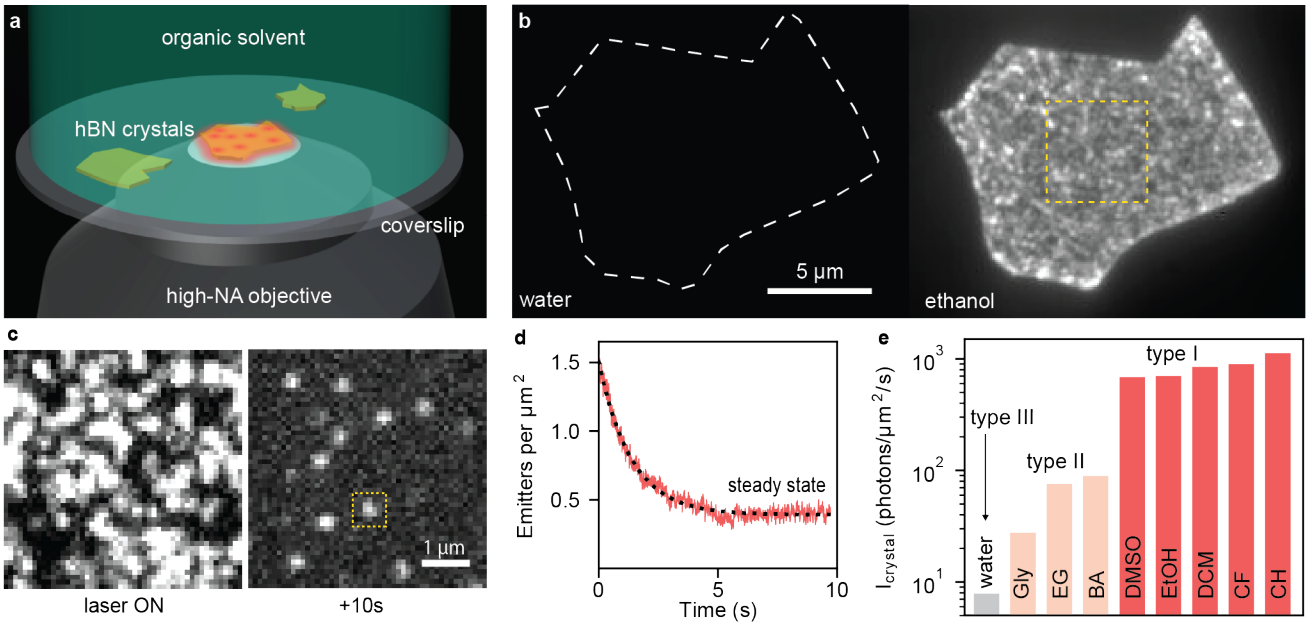


**Figure 1. Liquid-induced fluorescence from pristine hBN crystals**. **a**, Sketch of the experimental setup. **b**, Wide-field fluorescence images of an hBN crystal under 561 nm laser light illumination with 1 second exposure time. No fluorescence was observed in water, but in ethanol the entire crystal surface became fluorescent. **c** Zooming in the dashed yellow box in Fig. 1b, dense clusters of emission were observed upon turning the laser on (20 ms exposure per frame) in ethanol. After 10 seconds of wide-field illumination, the crystal surface reached a stable number of diffraction-limited isolated emitters. **d**, Localization microscopy-based counting of the emitters as a function of the illumination time: after 5 seconds, a steady state was reached. The dashed line is a fit to an offset exponential curve. **e**, Liquid dependency of the crystal fluorescence, showing strongly activating liquids (type I), mildly activating liquids (type II) and no activation in water (type III).

Considering the dynamics of these fluorescent emitters, a striking observation relates to the clear appearance of fluorescent trajectories at the surface of the crystal (see supplementary movie 2). These trajectories point to the correlated activation of neighbouring defects, corresponding to molecular random walks. By linking the super-resolved localization of defects (details in Methods), we can extract the associated trajectories, which are illustrated in Fig. 2b. These trajectories are similar to the ones observed on plasma-exposed hBN in water and binary mixtures of water and alcohols, which were attributed to proton hopping[20,21]. A similar phenomenology is thus expected here, with *(i)* defect activation due to reversible charge transfer from and to the solvent and *(ii)* correlated activation of neighbouring defects involving the motion of charge-bearing solvent molecules which remain physisorbed on the crystal surface while retaining lateral motion (as predicted for water ions[28]). However, the exact chemical mechanism must be distinct from what was proposed in water due to the aprotic nature of the solvents used here such as neat alkanes. As a comparison, the fluorescent signal in type I liquids is enhanced by over an order of magnitude with respect to plasma-treated hBN in water[20], and the spectral signature for the emission is distinct[20,21], pointing indeed to a different chemical mechanism, associated with a distinct defect type and reactivity. The chemical selectivity found in Fig. 1e suggests that a necessary and sufficient condition for a liquid molecule to activate native hBN defects is for it to bear a carbon atom in its chemical structure. This result is consistent with the recent finding that carbon plays a crucial role in

activating visible-range emitters in hBN[18].

By imaging a $\sim 13 \times 13 \mu m^2$ crystal area in the steady state for 50k, 6ms-long frames, we counted 700k localizations leading to 100k trajectories. We present in Fig. 2a a subset of these trajectories obtained from 5000 frames, overlaid with the super-resolved image from the same frames. This representation highlights that while the localization spots in some trajectories seem to hop freely, others remain trapped for long times resulting in bright spots in the super-resolved image. In other words, while most emitters only stay active for tens or hundreds of milliseconds, a fraction are found to be stable for several seconds (Fig. 2c) and we observed activations exceeding one minute (Fig. S6). Under typical illumination conditions ($\sim 3$ kW/cm$^2$), up to several thousand photons per defect per 20ms frame are counted, which is comparable to state-of-the-art fluorophores typically used for localization microscopy[29]. Therefore, liquid-activated solid-state defects act in a similar way as organic fluorophores without suffering from photobleaching, which is one of their main limitations.

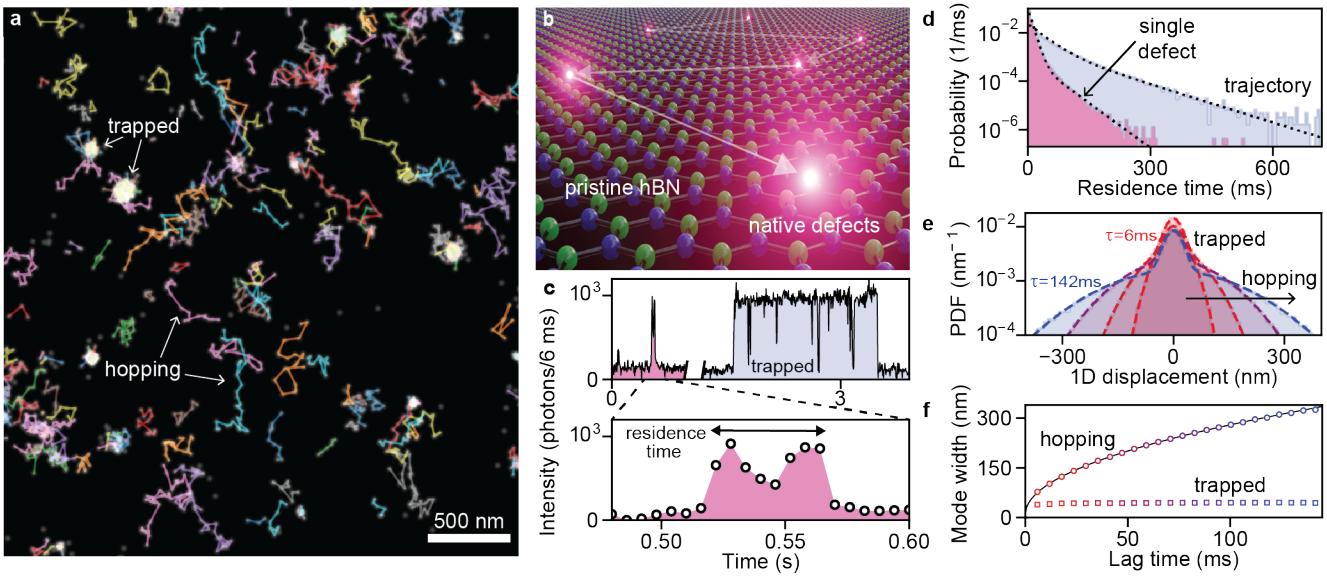


**Figure 2. Liquid-activated native hBN defects reveal interfacial molecular dynamics**. **a**, Overlay of a super-resolved image from 5000 frames showing hopping emitters in isopropanol as the linked trajectories, as well as trapped spots. **v**, Artist's view of the correlated activation of neighbouring defects leading to trajectories. **c**, Representative intensity traces from the same images, taken from 7x7 pixel bins around emitters as delimited by the dashed yellow box in Fig. 1c, with 6 ms exposure time. The top right trace corresponds to a long defect activation. The top left trace corresponds to a short activation of the same defect, magnified on the bottom panel. **d**, Distribution of residence times on single defects and for the entire trajectories. Dotted lines are fits to a two-component exponential decay. **e**, Displacement probability density function (PDF) of trajectories after different lag times $\tau$=6,24,66,142 ms. Dashed lines are fits to two-component Gaussians. **f**, Visualizing the evolution of the two modes of the Gaussian fit in Fig. 2e with increasing lag time. The central region, corresponding to the trapped state, remains of constant width, whereas the tails, corresponding to hopping, enlarge with time. The solid line is a fit to a standard diffusion curve.

To achieve further insight into the observed molecular random walks, we analyzed their statistical properties, with the emitter position described as a random variable of time $X(t)$, and the trajectory residence time on the crystal surface as another random variable $T_{\text{res}}^T$. As trajectory residence times comprise complex information on both the chemisorption energy at a single defects and the physisorption energy on pristine hBN in between defects, we also extracted residence times of molecules at single defect sites $T_{\text{res}}^D$ corresponding to chemisorption only. Both residence times were found to follow a double exponential decay (Fig. 2d), with slow exponential decay components $\tau_{\text{res}}^D$ =35 ms and $\tau_{\text{res}}^T$ =82 ms, respectively. Assuming that the defect residence time constant is given by the Arrhenius equation $\tau_{\text{res}}^D = \nu^{-1} e^{\Delta G/kT}$ where $\nu \approx 10^{12} - 10^{13}\, s^{-1}$ is a molecular attempt rate[21], we obtain a desorption free energy barrier $\Delta G \approx$ 24-27 kT$\approx$ 0.6-0.7 eV which is larger than typical physisorption

energies (tens of meV) and smaller than covalent bonding energies (several eV)[30]. This can be rationalized in terms of a lowered energy barrier under illumination[20], which is consistent with the observed light-induced reduction in number of emitters in Fig. 1d as well as the illumination dependency of the density of emitters (Fig. S5).

We now turn our attention to the dynamics of the random walks. For Brownian diffusion, the one-dimensional displacement probability distribution function given by $\mathrm{PDF}(x,\tau) = P\Big(X(t+\tau) - X(t) = x\Big)$ is a Gaussian distribution with size $\sqrt{2D\tau}$ where $D$ is the diffusion coefficient. Here we find that our random walks are best described instead by a two-component Gaussian model (Fig. 2e). The central part of the distribution, with size $\sim$20 nm, remains of constant size corresponding to the localization uncertainty when a trajectory is trapped. The tails of the distribution however enlarge with increasing lag time, characterizing hopping events. As shown in Fig. 2f, the scaling of the hopping tail size indeed follows Brownian diffusion with $D$= $9.1\times10^{-14}\mathrm{m}^2/\mathrm{s}$, that is 4 to 5 orders of magnitude slower than bulk liquid molecular diffusion coefficients. While this observation makes it impossible to resolve the molecular travel time between defects, it allows for imaging defect-mediated molecular dynamics with standard cameras of 10 ms time resolution, which we propose here as a tool for nanofluidics.

### Spectral properties

Having shown robust and intense fluorescence emission from type I liquid-activated hBN surface defects, we further studied the peculiar interactions between solid-state surface defects and the liquid phase by focusing on their spectral properties using spectral single-molecule localization microscopy (sSMLM)[27]. Briefly, the wide-field image signal is divided by a 50:50 beam splitter. Half of the signal is used for spatial SMLM introduced above, and the other half passes through a prism to decompose its wavelength components, allowing for simultaneous localization and spectral characterization, as shown in Fig. 3a. Summing over a large number of single-emitter spectra, ensemble averaged spectra are obtained (Fig. 3b). The single-emitter spectra were found to be homogeneously distributed, with the appearance of a single population of emitters when exposed to the same liquid environment. Spectra were consistently characterized by two peaks, the zero-phonon line (ZPL) and the phonon side band (PSB), which are typical of emitters embedded in a matrix.

Interestingly, these ensemble spectra appeared to depend strongly on the activating liquid, and more precisely on its static dielectric constant $\varepsilon_{\mathrm{liq}}$ - which remains valid up to the relevant GHz regime for solvents used here[31]. We present in Fig. 3b spectra of emitters obtained in the following liquids of increasing polarity: pentane (P), tert-butyl alcohol (TBA) and DMSO. A significant polarity-induced ZPL redshift of the defect emission spectrum was gradually observed from nonpolar pentane (615 nm) to more polar TBA (626 nm) to highly polar DMSO (641 nm). Beyond the ZPL shift, we observed changes in the PSB, which is less clearly defined for polar solvents. We report in Fig. 3c. the center wavelengths of both peaks as obtained from fitting to a two-Lorentzian model for a number of solvents ordered by increasing $\varepsilon_{\mathrm{liq}}$. We tested 1-pentanol (PA), isopropyl alcohol (IPA) and methanol (MeOH) on top of previously introduced liquids to interpolate dielectric constant values and found that both the ZPL and the PSB are redshifted by over 25 nm ( 80 meV) in highly polar liquids compared with nonpolar alkanes. In the range $\varepsilon_{\mathrm{liq}} < 25$, a linear dependence of the ZPL wavelength on the $\varepsilon_{\mathrm{liq}}$ was observed, with a slope close to 1 nm per dielectric constant unit, indicated by the dashed line (Fig. 3c).

This positive *solvatochromism* is expected to occur when the magnitude of the excited state dipole is larger than the ground state one, which is the case for $\pi - \pi^*$ transitions[32]. The Jablonski diagram presented in Fig. 3d. illustrates the process giving rise to the observed spectra. By absorbing a photon (excitation, green arrow), the defect is excited to a dipolar state which interacts with the solvent and relaxes without radiating (dipole relaxation, curved arrow). Direct evidence of the dipolar nature of our liquid-activated emitters is presented in Fig. 3e where PL changes were monitored while rotating either the linearly polarized light used for excitation (green) or the fluorescent signal from the defects (orange). Details are provided in Fig. S6. Similar dipolar excitation and emission was reported for several types of hBN defects[33,34]. As sketched in Fig. 3f, the solvatochromic redshift can be described by the presence of liquid molecular dipoles stabilizing the defect's excited state dipole, thus lowering its energy and redshifting the ZPL. After this step, the transition back to the ground state can occur in two ways: direct emission of a photon (ZPL, orange arrow), and phonon-assisted emission (PSB, red arrow), which is redshifted compared

to the ZPL as a fraction of the energy leads to lattice vibrations (phonon, zigzag arrow).

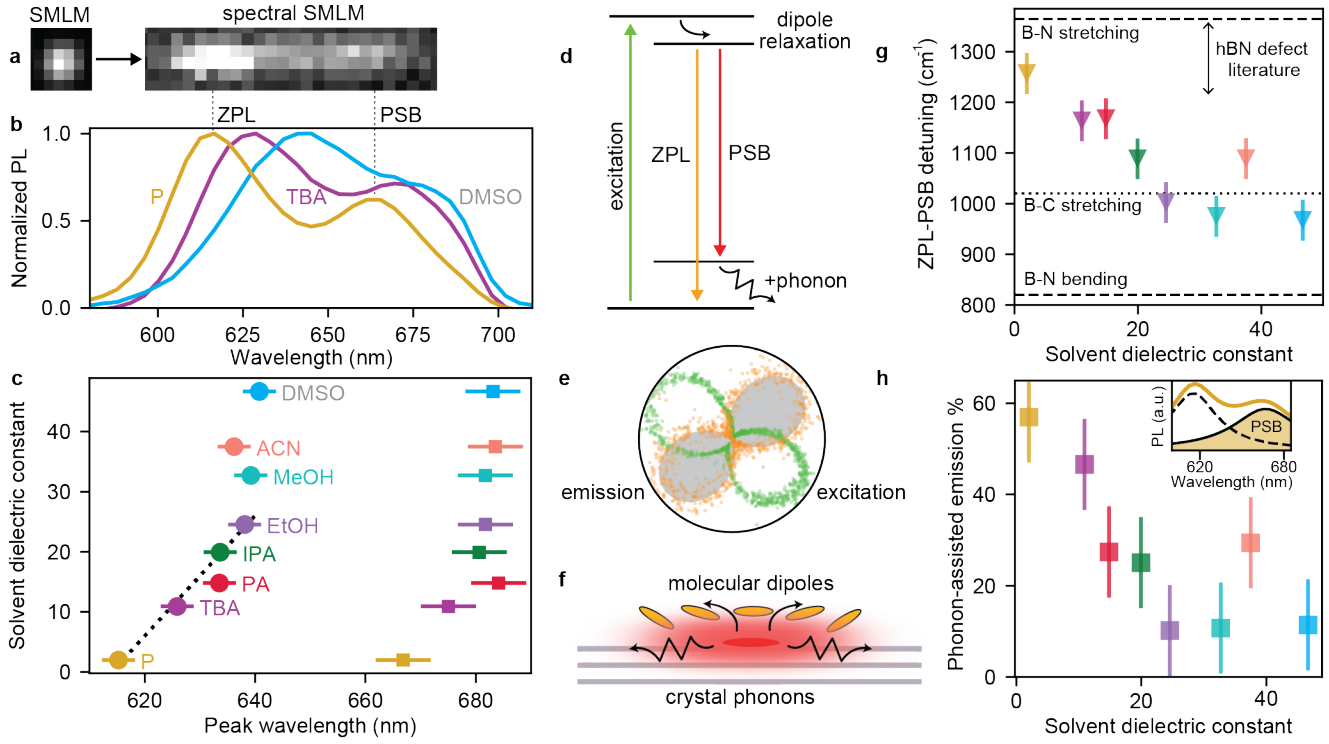


**Figure 3. Spectral properties of surface dipole emitters coupled to both crystal phonons and liquid environment**. **a**, Spectral single-molecule localization microscopy (sSMLM) splits the fluorescence signal from an emitter into a localization component (left) and a spectral component (right) on the same camera chip. **b**, Ensemble spectra of liquid-activated emitters in different type I solvents demonstrating a clear zero-phonon line (ZPL) and phonon side band (PSB). **c**, Visualizing the wavelength shifts of both ZPL (circles) and PSB (squares), which correlate with the dieletric constant of the liquid. Peak positions were obtained by fitting to a sum of Lorentzians. The dashed line indicates the linear solvatochromic range, with a slope of 1 nm per unit. **d**, Jablonski diagram of processes at play: 561 nm laser excitation induces a dipolar excited state, which can emit directly (orange arrow, ZPL) or with emission of a phonon (red arrow, PSB). **e**, Typical excitation and emission dipoles obtained from wide-field images. The shaded pattern corresponds to dipolar emission. The experimental procedure is detailed in Fig. S6. **f**, Sketch of an excited defect that can interact with both the crystal through phonons and with surrounding molecules (yellow ellipses). **g**, ZPL-PSB detuning as a function of the liquid dielectric constant, reporting on the phonon dispersion around defects. Dashed lines correspond to the Raman modes of hBN present in this energy range while the dotted line corresponds to B-C bonds as possible candidates for the observed vibrations. **h**, Quantifying the relative magnitude of phonon-assisted emission with respect to direct emission as a function of the solvent dielectric constant. The ratio is estimated as the area of the integrated PSB divided by the full integrated spectrum, as shown in the inset.

Continuing the analysis of the emission spectra, we evidence further peculiar interactions between the excited defect and solvent molecules. As shown in Fig. 3g, the energy difference between the ZPL and the PSB, which relates to the phonon dispersion of the material, was found to depend strongly on the solvent. The ZPL-PSB energy detuning ranges from 1250 $cm^{-1}$ for nonpolar pentane to 965 $cm^{-1}$ for polar DMSO, further hinting that the phonon emission is affected by the dipolar nature of the liquid medium. Classically, the phonon dispersion should peak at vibrational modes of the hBN crystal, shown as dashed lines. Around 1365 $cm^{-1}$ is the most intense vibrational mode of hBN, B-N stretching, which is both Raman and IR-active, and around 820 $cm^{-1}$ is the IR-active out-of-plane B-N bending mode[35–37]. The phonon side band of hBN defects PL spectra, which often arises in the 150-170 meV (1200-1400 $cm^{-1}$) detuning range, was attributed to B-N stretching previously[38,39]. While some variations were observed throughout the literature, to the best of our knowledge, vibrational modes below 1200 $cm^{-1}$ were not found in purely solid-state defects. Indeed, pristine hBN does not have any vibrational mode between 900 and

1200 $cm^{-1}$ which has been dubbed the 'phonon band gap' of hBN[40].

Various bonds could yield a phonon energy in this range: functionalization of hBN nanosheets with oxygen gives rise to IR-active modes in this range[41]. A recent theoretical study proposed that the chemisorption of carbon-bearing molecules on native hBN defects can give rise to vibrational modes precisely in the 900-1100 $cm^{-1}$ range[42]. The formation of B-C bonds seems particularly likely as they were found to occur around 1020 $cm^{-1}$ in boron-doped activated carbon[43] ,and carbon atoms are a common component of all activating solvents (type I and II). The apparent lowering in phonon energy with increasing solvent polarity could be explained by the progressive redistribution of emitted phonons from B-N stretching to B-C stretching. This comes with an overall decrease of the phonon-assisted emission from 60% down to 10%, quantified in Fig. 2h as the ratio of the integrated phonon side band over the integrated spectrum (inset). Overall, the vibrational signature of defects in organic solvents points toward covalent bonding between chemisorbed organic molecules and the defect centers. This mechanism is similar to the activation of emitters through the covalent bonding of molecules to carbon nanotubes[44]. However, as discussed in Fig. 2d, the residence time analysis at a defect suggests that this covalent bond is formed only transiently due to a decrease in desorption energy barrier by illumination.

### Room-temperature quantum emission in liquid

Liquid-activated native defects reported here host bright dipolar emission, with millions of photons emitted at trapping sites of the trajectories. The dipolar emission patterns shown in Fig. 3e suggest individual emitters, yet clusters of aligned emissive defects could exhibit the same pattern. To demonstrate that the measured fluorescence originates from single emitters, we performed time-correlated single-photon counting. For this, a 0.7 mW continuous-wave 561 nm laser beam was focused to a $\sim 1\mu m^2$ spot onto hBN crystals in liquid, and fluorescence signal was collected by two fiber-coupled single photon detectors (SPDs) in a Hanbury Brown and Twiss interferometer configuration (inset of Fig. 4a). The typical time trace of a stable single emitter in acetonitrile is shown in Fig. 4a. The observed photon count rate, close to a million counts per second, is comparable to previous reports[12]. As shown in Fig. 4b, the analysis of photon arrival times from a 10s-long trace in Fig. 4a exhibited a pronounced anticorrelation between both SPDs at zero delay time, which is the signature of non-classical, sub-Poissonian light. The extent of the photon antibunching dip $g^{(2)}(0) = 0.25 \pm 0.02$ without background correction shows unambiguously single-photon emission (SPE) from hBN defects in liquid. This result implies that the bright spots are single emitters and not clusters, thereby their optical readout truly reports on nanoscale properties of the liquid. The long-lasting emission thus stems from the strong chemisorption interaction between a single activating molecule and a single defect. The onset of quantum emission through the formation of a single covalent bond with a molecule was observed in carbon nanotubes[45], but the mechanism at play here exhibits the particularity of being fully reversible.

Photon statistical measurements were also performed with pulsed excitation, where the suppression of the correlated pulse peak at zero delay time, shown in Fig. 4c, confirmed single-photon emission. This feature did not depend on the activating liquid: it was also present in hexadecane with a measured $g^{(2)}(0) = 0.45 \pm 0.04$. The fluorescent lifetimes, corresponding to the width of the antibunching dip, were found to be 2.73$\pm$0.09 ns and 2.20 $\pm$ 0.20 ns for acetonitrile and hexadecane, respectively. Taking advantage of the solvatochromic shift reported in Fig. 3, we thus demonstrated liquid-tunable single-photon emission with a ZPL shift of $\sim$ 20 nm between hexadecane and acetonitrile, shown as an inset in Fig. 4b. The magnitude of the solvatochromic redshift (80 meV $\equiv$ 25 nm) is comparable with the most successful attempts to tune the single-photon emission of hBN defects through strain[46] or electrical control[47]. Such fine control of emitters at interfaces with liquid is appealing from both nanophotonic and nanofluidic perspectives: changes in the liquid environment may be translated into light signal, and conversely light control may be used to tune the properties of nanofluidic devices. Additional insights on spatial features of the quantum emission, including in the high-density regime may be gained by multi-detector quantum imaging with single-photon detector arrays[48].

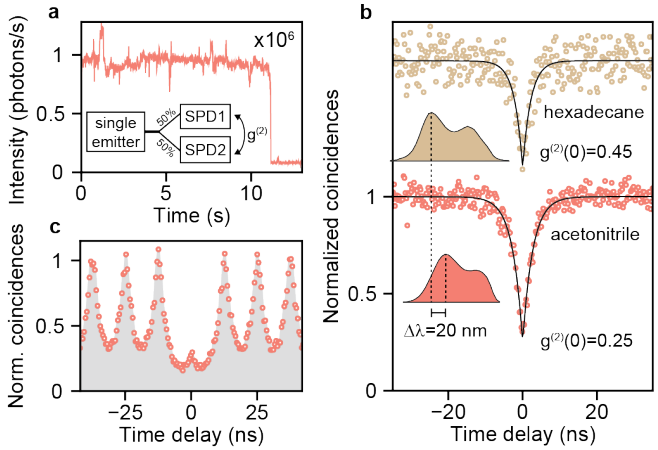


**Figure 4. Quantum emission from liquid-activated emitters**. **a**, Representative PL trace from an isolated emitter in acetonitrile under 700 $\mu$W confocal excitation. The shaded region corresponds to the 10s-long trace used for photon statistics. **b**, Second order correlation function $g^{(2)}(\tau)$ as measured from time correlated single photon counting in a Hanbury Brown and Twiss geometry, in hexadecane and acetonitrile. In both liquids, a pronounced antibunching is observed with $g^2(0) < 0.5$ without background correction, proving the non-classical nature of the emitted light. Spectra are shown in the inset, demonstrating liquid-tunable SPE from 620 nm to 640 nm. **c**, Single-photon statistics under pulsed laser excitation showing a suppression of the central peak due to antibunching.

### Integration in single-digit nanofluidic systems

Building upon this extensive spatial, temporal and spectral characterization of liquid-activated defects in pristine hBN, we then took advantage of layered van der Waals heterostructures to probe solid-liquid interfaces in molecular confinement. As sketched in Fig. 5a, we fabricated heterostructures comprising 3 crystals: bottom, spacer and top. The top crystal was chosen to be muscovite mica for its transparency and lack of fluorescent properties, and the bottom crystal was pristine hBN with native defects to be activated by the liquid. The middle layer, composed of few-layer graphene patterned by electron beam lithography, effectively acted as a spacer defining a slit between the hBN and mica sheets, whose height is set by the number of $\sim 3.4$ Å-thick graphene layers[4]. Fabrication details are provided in Methods and in Fig. S7.

An optical micrograph of a device with $h = 2.4$ nm is provided in Fig. 5c. The bottom green region corresponds to the full heterostructure with nanoslits, and the top region corresponds to the open hBN flake masked by graphene spacers but without encapsulation by the mica. We first verified that covering the pristine hBN crystal with a patterned few-layer graphene crystal masks liquid-activated defects, as was observed for other types of hBN defects.[49,50] As shown in Fig. S8, emitters on bare hBN are randomly distributed, but the graphene mask allows for the precise positioning of emitters on the basal plane of hBN in liquid. An overlay of the graphene spacer atomic force microscopy (AFM) topography and the super-resolved image is shown in Fig. 5b, demonstrating the correspondence between the lithographically defined graphene pattern and the optically measured fluorescence from masked hBN defects. We further verified that capping the masked defects with mica does not quench their fluorescence, allowing direct imaging of defects in a confined liquid (Fig. 5d). We show in Fig. 5e that the localization intensity distributions with and without the confining mica top are similar, but the number of emitters in confinement is reduced by two thirds.

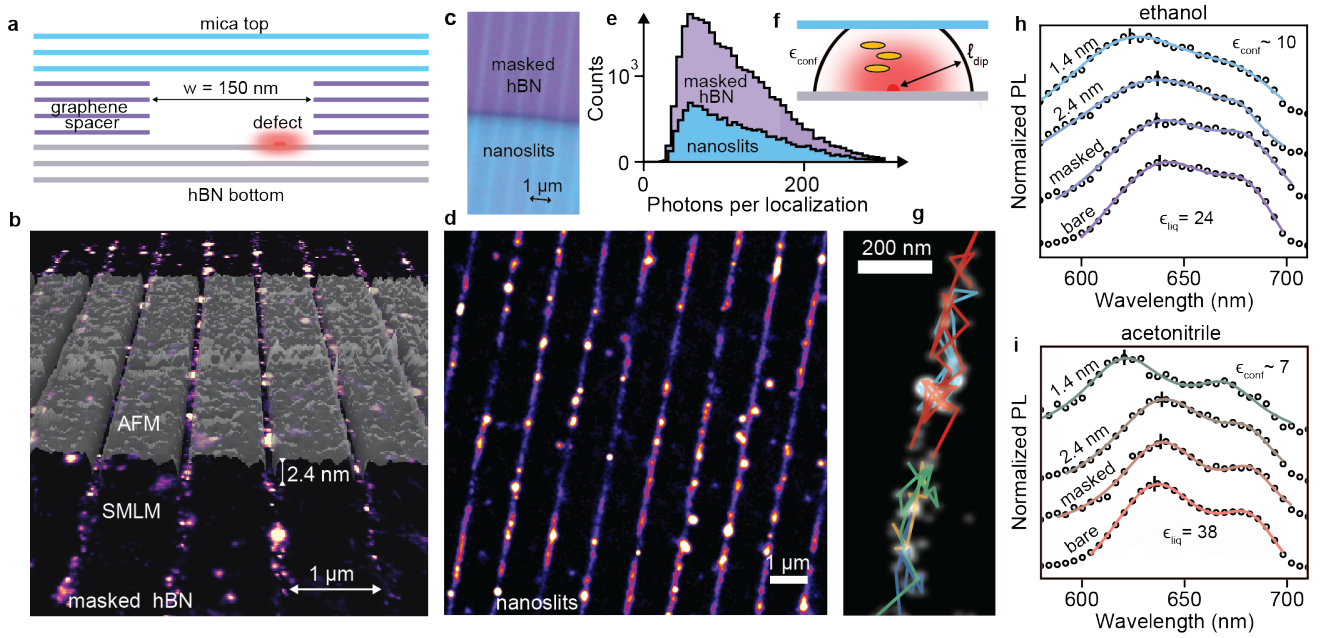


**Figure 5. Nanoslit-embedded liquid-activated emitters**. **a**, Sketch of the 3-layer heterostructure nanochannel device. The red glow indicates a liquid-activated defect inside the nanoslit. **b**, Overlay of a super-resolved image of masked ethanol-activated hBN and the AFM mapping of the graphene spacers. **c**, Optical micrograph of the heterostructure. On top only two layers of the heterostructure are present: graphene spacers on the hBN bottom crystal, realizing masked hBN. The bottom blue region corresponds to the full heterostructure with channels. **d**, Super-resolved image of acetonitrile-activated defects embedded in 2.4 nm-high nanoslits, from 30k frames with 20 ms exposure time and 1.4 kW/cm$^2$ illumination. **e**, Comparison of localization intensity distributions for masked hBN and 2.4 nm nanoslits in acetonitrile, showing that there was no loss of photons per event but an overall reduction in number of localizations. The counting procedure is detailed in Fig. S9. **f**, Illustration of the effect of confinement: the liquid dielectric constant can be changed by confinement ($\varepsilon_{\text{conf}}$) and the defect dipole interacts with solvent molecules (yellow ellipses) within a range $\ell_{\text{dip}}$, comparable to the confinement size $h$. **g**, Representative trajectories in 2.4 nm-high nanoslits filled with ethanol, overlaid with the super-resolved image. **h,i**, sSMLM spectra of liquid-activated defects in nanoslits filled with ethanol and acetonitrile, respectively. The confinement size is tuned from the open geometry to 2.4 nm down to 1.4 nm. Solid lines correspond to two-component Lorentzian fits, and black dashes indicate the extracted ZPL position.

Integrating defects into nanofluidic channels now represents a unique opportunity to probe the effect of confinement on liquid structure and dynamics. We first confirm the observation of trajectories in 1.4 nm confinement in Fig. 5g, where a set of emitters is shown to explore the $\sim$ 150 nm-wide channel. We then focus on the spectral properties of confined emitters, which can be robustly extracted through sSMLM with relatively low numbers of localizations (<1000). We present sSMLM spectra obtained in the bare, masked and confined geometries for ethanol (Fig. 5g) and acetonitrile (Fig. 5h). For both solvents, bringing the confinement size from 2.4 nm down to 1.4 nm leads to a clear blueshift pinpointed by the dashes indicating the ZPL position. For ethanol, the ZPL blueshifts from 638 nm to $\sim$ 624 nm, and for acetonitrile, transitions from 636 nm to $\sim$621 nm under 1.4 nm confinement, bringing the spectral signature of a strongly polar solvent close to that of nonpolar alkanes. This substantial confinement-induced blueshift suggests that emitters experience a reduced dielectric constant of $\varepsilon_{\text{conf}}$ $\sim$10 in ethanol and $\sim$7 in acetonitrile when considering Fig. 3c as a calibration curve.

Bringing the top mica wall close to the defects may affect their emission in two ways. First, the wall with lowered dielectric constant ($\varepsilon_{\text{wall}} \approx 8$)[51] may deplete the shell of solvent dipoles interacting with the defect and confine field lines within the channel[52], thereby destabilizing the excited state. Second, a more indirect way of affecting the emission is by reducing the out-of-plane component of the dielectric constant tensor[7]. As sketched in Fig. 5f the range of interaction between a solvent molecule with dipole $\mu_S$ and the defect with dipole $\mu_D$ is $\ell_{\text{dip}} = (\mu_S \mu_D / 2\pi\varepsilon_o k_B T)^{1/3}$. With the coarse assumption that

$\mu_D \sim a \times e$ where $a \approx 0.25$ nm is the in-plane lattice parameter of hBN and $e$ is the unit charge, we obtain $\mu_D \approx 12$ D. Based on the dipole moments of ethanol (1.7 D) and acetonitrile (3.4 D) we obtain $\ell_{\mathrm{dip}} \approx 1$ nm and 1.3 nm, respectively, which is smaller than the set nanoslit height. Therefore, it seems unlikely that the observed effect under 1.4 nm confinement should arise purely from the top wall depleting the interacting dipole shell around the defect (bottom), and our results may be explained by the confinement-induced reduction of the solvent dielectric constant as was observed for water[7] and predicted for other liquids[53].

Overall, these results consolidate the picture of dipolar environment-tuned defects, whose properties are affected by changes in the sensing hemisphere with volume $\sim 2/3\pi\ell_{\mathrm{dip}}^3$, which encloses fewer than 100 molecules in the case of acetonitrile. Beyond passive diffusion and dielectric sensing of confined liquids, tracking defect activation dynamics in confinement may be used to directly image nanoscale flow and study its interplay with defects[54]. While a macroscopic control over the ensemble surface charge of nanofluidic devices with light was found to be useful for biomolecule detection[55] and energy harvesting applications[56,57], the possibility to address single charges in confinement suggested by our results may reveal fundamentally new phenomena such as correlated ion transport[52].

## Conclusions

In summary, defects in hBN crystals, already known for a variety of outstanding optical properties, were found to exhibit a peculiar interaction with liquids. Indeed, native point defects on the atomically smooth surface of the as-exfoliated crystal become emissive when in contact with organic solvents. This unique system, where the encounter of a single defect with a single organic molecule yields a single-photon emitter, reconciles solid-state emitters and organic fluorophores to constitute a new tool for the study of solid-liquid interfaces. We demonstrated two directions for sensing with liquid-activated hBN defects: activation dynamics report on interfacial single-charge transfer between defects, while the bright emission spectra of emitters offer a readout of their nanoscale dielectric surrounding. These phenomena were found to hold in single-digit nanometer confinement, allowing for the design of liquid-responsive nanostructures that may find useful applications for the optical imaging of molecular interactions at solid-liquid interfaces in nanofluidic systems *operando*.

## Methods

### Sample preparation

Pristine hBN flakes from high-quality crystals[24] were exfoliated onto glass coverslips (no. 1.5 Micro Coverglass, Electron Microscopy Sciences, 25 mm in diameter), using standard blue tape. High-quality crystals purchased from HQ Graphene were also tested and exhibited no notable difference with samples grown by the authors. The crystals were immersed immediately following exfoliation, and the chamber was thoroughly rinsed three times at each solvent exchange with fresh solvent. Solvents used are detailed in supplementary section 1.

The slit-shaped nanochannel is made of a tri-crystal van der Waals (vdW) heterostructure of a spacer layer sandwiched between a top layer and a bottom layer following the same protocol as previously reported[4]. Here, the vdW stack is composed of top mica-graphene spacer-bottom hBN. In brief, thin layered graphene was first patterned via EBL into parallel strips with a width of 1 µm and a separation of 150 nm. A mica crystal ($\sim$ 200 nm thick) was then transferred on top of the graphene spacer, via PMMA based transfer method. Then this mica-graphene spacer stack was lifted and transferred onto a freshly exfoliated hBN layer. This whole stack was then transferred onto a glass coverslip for the imaging. The channel dimensions of the final device is shown in Figure 5a where it has a width of $\sim$ 150 nm, a length of 20 µm and a height equivalent to the thickness of the graphene spacer. Fabrication flow chart and material requirements are described in detail in supplementary Figure S7.

### Optical microscopy

Widefield imaging was performed on a custom wide-field fluorescence microscope, described elsewhere[27]. Briefly, the emitters are excited using 561 nm laser (Monolithic Laser Combiner 400B, Agilent Technologies), which is collimated and focused on the back focal plane of a high-numerical aperture oil-immersion microscope objective (Olympus TIRFM 100X, NA: 1.45). This

configuration leads to wide-field illumination of the sample in a circle with $\approx 25\mu m$ diameter. Fluorescence emission from the sample is collected by the same objective and spectrally separated from the excitation light using dichroic and emission filters (ZT488/561rpc-UF1 and ZET488/561m, Chroma) before being projected on an EMCCD camera (Andor iXon Life 897) with EM gain of 150. An additional spectral path, mounted in parallel to the localization path allows for simultaneous measurements of the emission spectra from individual emitters (see details below). The sample itself is mounted in a sealed fluidic chamber, which is placed on a piezoelectric scanner (Nano-Drive, MadCityLabs) for fine focus. Typical exposure time is 20-50 ms and typical laser power 10-100 mW for the widefield excitation area of $2\times10^3$ $\mu m^2$, resulting in a power density of $0.35-3.5$ kW$/cm^2$. A typical acquired image stack contained 2-10 thousand frames.

Confocal microscopy measurements were performed in an inverted microscope configuration allowing to image samples in liquid. Here the emission was split between two fiber-coupled APDs (SPCM-AQRH, Excelitas) in an Hanbury Brown and Twiss configuration. Photon correlation measurements were performed using the PicoHarp TCSPC module (PicoQuant). Python package Qudi[58] was used for data analysis.

### Spectral SMLM procedure

Acquired image stacks from the wide-field microscope were processed using ThunderSTORM[59]. Spatial SMLM for emitter counting, super-resolution image rendering and trajectory analysis was performed by filtering localization events with $30 < \sigma_{PSF} < 200$ nm. SMLM localization events were rendered as 2D gaussians with a standard deviation of 20 nm unless specified otherwise, reflecting the uncertainty on the emitter's position.

Spectral SMLM (sSMLM) was performed following a procedure described elsewhere[27] with few modifications: the spectra were directly extracted through a spatial matrix transformation. Spatial localization events were filtered by intensity to ensure readable spectra (threshold set to 300 photons per localization) and sigma (between 30 and 200 nm) before analyzing the corresponding spectra. Overlapping spectra were excluded when computing the ensemble spectrum.

Ensemble sSMLM spectra were fit using Python package LMFIT[60], to a model composed of 2 Lorentzians corresponding to the ZPL and PSB and a constant background. As shown in Fig. 5g-h, only the part of the normalized signal emerging more than 20% over the background was fit, as the background-induced spectra tails could pose fitting issues. For spectra in nanoslits, a spatial filter was applied to avoid counting signal from contaminations in between channels (details in Fig. S9).

### Trajectory linking

Wide-field fluorescence frames acquired with the EMCCD camera were first localized using ThunderSTORM[59] with parameters described in Methods. Trajectories were obtained by applying the Crocker-Grier linking algorithm[61] to the localization microscopy tables. Briefly, for each localization event at a given frame, the algorithm will link another event if it is found at the next frame within a specified search range. This search range was set to 120 nm in Fig. 2, as the probability of having a 1D displacement exceeding this value is less than 1% according to the analysis in Fig. 1e. The Python package Trackpy[62] was used for the implementation of the linking.

### Uncertainty estimations

Typical uncertainty of the ZPL and PSB position were estimated on the order of 3 and 5 nm, respectively (Fig. 3c). The fitting uncertainty is typically smaller than 1 nm, and the assigned uncertainty value reflects measurement-to-measurement variations. For the ZPL-PSB detuning, the error bars were estimated following the same procedure to 80 cm$^{-1}$ (Fig.3g). For the phonon-assisted emission estimation, the leading uncertainty component corresponds to the evaluation of the height of the peak, which can reach up to 10% (Fig. 3h).

## Acknowledgements

This work was financially supported by the European Research Council (grant no. 101020445), the Swiss National Science Foundation (grant no. 200021 192037) and the CCMX Materials Challenge grant "Large area growth of 2D materials for

device integration". B.R. acknowledges the funding from Royal Society University Research Fellowship URF/R1/180127. B.R., Y.Y., G-H.N acknowledge funding from the European Union's H2020 Framework Programme/ERC Starting Grant agreement number 852674 - AngstroCAP, and RS enhancement award RF/ERE/210016. A.K. acknowledges the funding from the Royal Society International Exchanges Award, IES/R1/201028 and EPSRC new horizons grant EP/V048112/1. K.W. and T.T. acknowledge support from the JSPS KAKENHI (Grant Numbers 19H05790, 20H00354 and 21H05233). N.R. acknowledges useful conversations with Marie-Laure Bocquet and Vasily Artemov.

## Author contributions

N.R. observed the effect. A.R., B.Ra., J.C., A.K. and N.R. conceived the defect integration in nanoslits; A.R., N.R., M. L., T.-H. C., B.Ra., A.K. and J.C. designed experiments; E.G. fabricated the marked coverslips. Y. Y. and G.-H. N. fabricated the nanoslit devices under the supervision of B.Ra. and A. K.; N.R. performed sSMLM measurements. N.R. performed confocal microscopy measurements with the assistance of E.G.; N.R. analyzed the data and interpreted it with the help of J.C., E.G., M.L., B.Re. and A.R. ; K.W. and T.T. contributed materials; N.R. wrote the paper with the assistance of J.C. and inputs from all authors; A.R. supervised the project; All authors discussed the results and commented on the manuscript.

## Data availability

The data that support the findings of this study are available from the corresponding authors on reasonable request.

## Competing interests

The authors declare no competing interests.

## Additional information

Supplementary information is available in the online version of the paper.

## References

1. Faucher, S. *et al.* Critical knowledge gaps in mass transport through single-digit nanopores: A review and perspective. *The J. Phys. Chem. C* **123**, 21309–21326 (2019).
2. Bocquet, L. Nanofluidics coming of age. *Nat. Mater.* **19**, 254–256 (2020).
3. Majumder, M., Chopra, N., Andrews, R. & Hinds, B. J. Enhanced flow in carbon nanotubes. *Nature* **438**, 44–44 (2005).
4. Radha, B. *et al.* Molecular transport through capillaries made with atomic-scale precision. *Nature* **538**, 222–225 (2016).
5. Mouterde, T. *et al.* Molecular streaming and its voltage control in ångström-scale channels. *Nature* **567**, 87–90 (2019).
6. Agrawal, K. V., Shimizu, S., Drahushuk, L. W., Kilcoyne, D. & Strano, M. S. Observation of extreme phase transition temperatures of water confined inside isolated carbon nanotubes. *Nat. Nanotechnol.* **12**, 267–273 (2017).
7. Fumagalli, L. *et al.* Anomalously low dielectric constant of confined water. *Science* **360**, 1339–1342 (2018).
8. Grimm, J. B. & Lavis, L. D. Caveat fluorophore: an insiders' guide to small-molecule fluorescent labels. *Nat. Methods* **19**, 149–158 (2022).
9. Wong, D. *et al.* Characterization and manipulation of individual defects in insulating hexagonal boron nitride using scanning tunnelling microscopy. *Nat. Nanotechnol.* **10**, 949–953 (2015).
10. Schirhagl, R., Chang, K., Loretz, M. & Degen, C. L. Nitrogen-vacancy centers in diamond: nanoscale sensors for physics and biology. *Annu. Rev. Phys. Chem.* **65**, 83–105 (2014).
11. Wolfowicz, G. *et al.* Quantum guidelines for solid-state spin defects. *Nat. Rev. Mater.* **6**, 906–925 (2021).

**12.** Tran, T. T., Bray, K., Ford, M. J., Toth, M. & Aharonovich, I. Quantum emission from hexagonal boron nitride monolayers. *Nat. Nanotechnol.* **11**, 37–41 (2016).

**13.** Hayee, F. *et al.* Revealing multiple classes of stable quantum emitters in hexagonal boron nitride with correlated optical and electron microscopy. *Nat. Mater.* **19**, 534–539 (2020).

**14.** Kianinia, M., Xu, Z.-Q., Toth, M. & Aharonovich, I. Quantum emitters in 2D materials: Emitter engineering, photophysics, and integration in photonic nanostructures. *Appl. Phys. Rev.* **9**, 011306 (2022).

**15.** Choi, S. *et al.* Engineering and localization of quantum emitters in large hexagonal boron nitride layers. *ACS Appl. Mater. &Interfaces* **8**, 29642–29648 (2016).

**16.** Fournier, C. *et al.* Position-controlled quantum emitters with reproducible emission wavelength in hexagonal boron nitride. *Nat. Commun.* **12**, 1–6 (2021).

**17.** Proscia, N. V. *et al.* Near-deterministic activation of room-temperature quantum emitters in hexagonal boron nitride. *Optica* **5**, 1128–1134 (2018).

**18.** Mendelson, N. *et al.* Identifying carbon as the source of visible single-photon emission from hexagonal boron nitride. *Nat. Mater.* **20**, 321–328 (2021).

**19.** Qiu, Z. *et al.* Atomic structure of carbon centres in hBN: towards engineering of single photon sources. *arXiv preprint arXiv:2110.07842* (2021).

**20.** Comtet, J. *et al.* Direct observation of water-mediated single-proton transport between hBN surface defects. *Nat. Nanotechnol.* **15**, 598–604 (2020).

**21.** Comtet, J. *et al.* Anomalous interfacial dynamics of single proton charges in binary aqueous solutions. *Sci. Adv.* **7**, eabg8568 (2021).

**22.** Glushkov, E. *et al.* Engineering optically active defects in hexagonal boron nitride using focused ion beam and water. *ACS Nano* **16**, 3695–3703 (2022).

**23.** Na, Y. S. *et al.* Modulation of optical and electrical properties in hexagonal boron nitride by defects induced via oxygen plasma treatment. *2D Mater.* **8**, 045041 (2021).

**24.** Taniguchi, T. & Watanabe, K. Synthesis of high-purity boron nitride single crystals under high pressure by using Ba–BN solvent. *J. Cryst. Growth* **303**, 525–529 (2007).

**25.** Schué, L., Stenger, I., Fossard, F., Loiseau, A. & Barjon, J. Characterization methods dedicated to nanometer-thick hBN layers. *2D Mater.* **4**, 015028 (2016).

**26.** Henck, H. *et al.* Direct observation of the band structure in bulk hexagonal boron nitride. *Phys. Rev. B* **95**, 085410 (2017).

**27.** Comtet, J. *et al.* Wide-field spectral super-resolution mapping of optically active defects in hexagonal boron nitride. *Nano Lett.* **19**, 2516–2523 (2019).

**28.** Grosjean, B., Bocquet, M.-L. & Vuilleumier, R. Versatile electrification of two-dimensional nanomaterials in water. *Nat. Commun.* **10**, 1–8 (2019).

**29.** Dempsey, G. T., Vaughan, J. C., Chen, K. H., Bates, M. & Zhuang, X. Evaluation of fluorophores for optimal performance in localization-based super-resolution imaging. *Nat. Methods* **8**, 1027–1036 (2011).

**30.** Huber, F. *et al.* Chemical bond formation showing a transition from physisorption to chemisorption. *Science* **366**, 235–238 (2019).

**31.** Yomogida, Y., Sato, Y., Nozaki, R., Mishina, T. & Nakahara, J. Dielectric study of normal alcohols with THz time-domain spectroscopy. *J. Mol. Liq.* **154**, 31–35 (2010).

**32.** Nigam, S. & Rutan, S. Principles and applications of solvatochromism. *Appl. Spectrosc.* **55**, 362A–370A (2001).

**33.** Jungwirth, N. R. *et al.* Temperature dependence of wavelength selectable zero-phonon emission from single defects in hexagonal boron nitride. *Nano Lett.* **16**, 6052–6057 (2016).

**34.** Jungwirth, N. R. & Fuchs, G. D. Optical absorption and emission mechanisms of single defects in hexagonal boron nitride. *Phys. Rev. Lett.* **119**, 057401 (2017).

**35.** Geick, R., Perry, C. & Rupprecht, G. Normal modes in hexagonal boron nitride. *Phys. Rev.* **146**, 543 (1966).

**36.** Reich, S. *et al.* Resonant raman scattering in cubic and hexagonal boron nitride. *Phys. Rev. B* **71**, 205201 (2005).

**37.** Serrano, J. *et al.* Vibrational properties of hexagonal boron nitride: inelastic X-ray scattering and ab initio calculations. *Phys. Rev. Lett.* **98**, 095503 (2007).

**38.** Chejanovsky, N. *et al.* Structural attributes and photodynamics of visible spectrum quantum emitters in hexagonal boron nitride. *Nano Lett.* **16**, 7037–7045 (2016).

**39.** Martínez, L. *et al.* Efficient single photon emission from a high-purity hexagonal boron nitride crystal. *Phys. Rev. B* **94**, 121405 (2016).

**40.** Vuong, T. *et al.* Phonon-photon mapping in a color center in hexagonal boron nitride. *Phys. Rev. Lett.* **117**, 097402 (2016).

**41.** Sainsbury, T. *et al.* Oxygen radical functionalization of boron nitride nanosheets. *J. Am. Chem. Soc.* **134**, 18758–18771 (2012).

**42.** Jiang, T., Le, D., Rawal, T. B. & Rahman, T. S. Syngas molecules as probes for defects in 2D hexagonal boron nitride: their adsorption and vibrations. *Phys. Chem. Chem. Phys.* **23**, 7988–8001 (2021).

**43.** Romanos, J. *et al.* Infrared study of boron–carbon chemical bonds in boron-doped activated carbon. *Carbon* **54**, 208–214 (2013).

**44.** Piao, Y. *et al.* Brightening of carbon nanotube photoluminescence through the incorporation of sp3 defects. *Nat. Chem.* **5**, 840–845 (2013).

**45.** He, X. *et al.* Tunable room-temperature single-photon emission at telecom wavelengths from sp3 defects in carbon nanotubes. *Nat. Photonics* **11**, 577–582 (2017).

**46.** Mendelson, N., Doherty, M., Toth, M., Aharonovich, I. & Tran, T. T. Strain-induced modification of the optical characteristics of quantum emitters in hexagonal boron nitride. *Adv. Mater.* **32**, 1908316 (2020).

**47.** Nikolay, N. *et al.* Very large and reversible Stark-shift tuning of single emitters in layered hexagonal boron nitride. *Phys. Rev. Appl.* **11**, 041001 (2019).

**48.** Lubin, G. *et al.* Quantum correlation measurement with single photon avalanche diode arrays. *Opt. Express* **27**, 32863–32882 (2019).

**49.** Xu, Z.-Q. *et al.* Charge and energy transfer of quantum emitters in 2D heterostructures. *2D Mater.* **7**, 031001 (2020).

**50.** Stewart, J. C. *et al.* Quantum emitter localization in layer-engineered hexagonal boron nitride. *ACS Nano* **15**, 13591–13603 (2021).

**51.** Weeks Jr, J. The dielectric constant of mica. *Phys. Rev.* **19**, 319 (1922).

**52.** Kavokine, N., Marbach, S., Siria, A. & Bocquet, L. Ionic Coulomb blockade as a fractional Wien effect. *Nat. Nanotechnol.* **14**, 573–578 (2019).

**53.** Motevaselian, M. H. & Aluru, N. R. Universal reduction in dielectric response of confined fluids. *ACS Nano* **14**, 12761–12770 (2020).

**54.** Seal, A. & Govind Rajan, A. Modulating water slip using atomic-scale defects: Friction on realistic hexagonal boron nitride surfaces. *Nano Lett.* **21**, 8008–8016 (2021).

**55.** Di Fiori, N. *et al.* Optoelectronic control of surface charge and translocation dynamics in solid-state nanopores. *Nat. Nanotechnol.* **8**, 946–951 (2013).

**56.** Xiao, K. *et al.* Artificial light-driven ion pump for photoelectric energy conversion. *Nat. Commun.* **10**, 1–7 (2019).

**57.** Graf, M. *et al.* Light-enhanced blue energy generation using mos2 nanopores. *Joule* **3**, 1549–1564 (2019).

**58.** Binder, J. M. *et al.* Qudi: A modular python suite for experiment control and data processing. *SoftwareX* **6**, 85–90 (2017).

**59.** Ovesnỳ, M., Křížek, P., Borkovec, J., Švindrych, Z. & Hagen, G. M. ThunderSTORM: a comprehensive ImageJ plug-in for PALM and STORM data analysis and super-resolution imaging. *Bioinformatics* **30**, 2389–2390 (2014).

**60.** Newville, M., Stensitzki, T., Allen, D. B. & Ingargiola, A. LMFIT: Non-Linear Least-Square Minimization and Curve-Fitting for Python, DOI: 10.5281/zenodo.11813 (2014).

**61.** Crocker, J. C. & Grier, D. G. Methods of digital video microscopy for colloidal studies. *J. Colloid Interface Sci.* **179**, 298–310 (1996).

**62.** Allan, D. B., Caswell, T., Keim, N. C., van der Wel, C. M. & Verweij, R. W. soft-matter/trackpy: Trackpy v0.5.0, DOI: 10.5281/zenodo.4682814 (2021).